





Article

Magnetic Nanoparticles of Fe_3O_4 Biosynthesized by *Cnicus benedictus* Extract: Photocatalytic Study of Organic Dye Degradation and Antibacterial Behavior

Álvaro de Jesús Ruíz-Baltazar ^{1,*}, Nestor Méndez-Lozano ², Daniel Larrañaga-Ordáz ^{2,3},
Simón Yobanny Reyes-López ⁴, Marco Antonio Zamora Antuñano ² and
Ramiro Pérez Campos ⁵

¹ CONACYT-Centro de Física Aplicada y Tecnología Avanzada, Universidad Nacional Autónoma de México, Boulevard Juriquilla 3001, Santiago de Querétaro 76230, Mexico

² Universidad del Valle de México, Campus Querétaro, Naranjos Punta Juriquilla 1000, Santa Rosa Jáuregui, Santiago de Querétaro 76230, Mexico; nestor.mendez@uvmnet.edu (N.M.-L.); daniel.larranaga@fata.unam.mx (D.L.-O.); marco.zamora@uvmnet.edu (M.A.Z.A.)

³ Centro de Física Aplicada y Tecnología Avanzada, Universidad Nacional Autónoma de México, Boulevard Juriquilla 3001, Santiago de Querétaro 76230, Mexico

⁴ Instituto de Ciencias Biomédicas, Universidad Autónoma de Ciudad Juárez, Envolverte del PRONAF y Estocolmo s/n, Ciudad Juárez, CHIC., México CP 32300, Mexico; simon.reyes@uacj.mx

⁵ Instituto de Ciencias Físicas, Universidad Nacional Autónoma de México, Av Universidad s/n, Col. Chamilpa, Cuernavaca 62210, Mexico; ramirop21@gmail.com

* Correspondence: aruizbaltazar@fata.unam.mx

Received: 10 July 2020; Accepted: 1 August 2020; Published: 6 August 2020



Abstract: Currently, the use of sustainable chemistry as an ecological alternative for the generation of products or processes that are free of a polluting substance has assumed a preponderant role. The aim of this work is to propose a bioinspired, facile, low cost, non-toxic, and environmentally friendly alternative to obtaining magnetic nanoparticles with a majority phase of magnetite (Fe_3O_4). It is important to emphasize that the synthesis was based on the chemical reduction through the *Cnicus benedictus* extract, whose use as reducing agent has not been reported in the synthesis of iron oxides nanoparticles. In addition, the *Cnicus benedictus* is an abundant endemic plant in Mexico with several medicinal properties and a large number of natural antioxidants. The obtained nanoparticles exhibited significant magnetic and antibacterial properties and an enhanced photocatalytic activity. The crystallite size of the Fe_3O_4 nanoparticles (Fe_3O_4 NP's) was calculated by the Williamson-Hall method. The photocatalytic properties of the Fe_3O_4 NP's were studied by kinetics absorptions models in the Congo red (CR) degradation. Finally, the antibacterial effects of the Fe_3O_4 NPs were evaluated mediated the Kirby–Bauer method against *Escherichia coli* and *Staphylococcus aureus* bacteria. This route offers a green alternative to obtain Fe_3O_4 NPs with remarkable magnetic, photocatalytic, and antibacterial properties.

Keywords: iron oxides; nanoparticles; organic dye degradation; photocatalytic effect antibacterial behavior

1. Introduction

In recent years, the development of new nanomaterials and nanoscience study has cobranded a preponderant place due to the wide number of researchers in those fields. This is due to the notables physical, chemical, magnetic, optical, electronic, and catalytic properties exhibited by the materials at the nanometric scale [1–3]. The quantic confinement of the atoms on the nanoparticles favors the reactivity

of the nanoparticles, which results in better properties associated with the nanoparticles in comparison to the bulk materials. Specifically, the Fe_3O_4 nanoparticles have been employed in several applications including magnetic resonance imaging (MRI), hyperthermia, drug delivery, heterogeneous catalysis, photocatalysis, magnetic carriers, and wastewater treatment [4–10]. Some synthesis methodologies for obtaining Fe_3O_4 such as co-precipitations and thermal decomposition have been reported as more common [11,12]. However, in many cases, the mentioned methods involve the use of surfactants, reducing agents, and organic solvents, which are toxic, expensive, and have a negative environmental impact [13–15]. In this sense, the new directrix for the synthesis of Fe_3O_4 nanoparticles is focused on the green chemical. Organic and biocompatible molecules such as vitamin B12, glucose cellulose, amino acids, and even plant extracts have been employed as stabilizing and/or reducing agents [16–20]. It is important to emphasize that the search for new alternatives that promote sustainable chemistry has become a priority issue. In this sense, endemic plants offer a sustainable and functional alternative to obtain nanomaterials [21–23]. On the other hand, it is well known that, in recent years, the use of plants as reducing agents (*Myzus persicae*, *Ceratonia siliqua*, *Calotropis gigantea*, *Thymus kotschyianus* leaf extract, and *Pisum sativum* peels) during the chemical synthesis of Fe_3O_4 nanoparticles has been widely reported [24–31]. However, the diversity of plants, properties, and compounds present in each species is very wide, and interaction in the synthesis process is reflected in the properties of the nanomaterials obtained. Therefore, it is important to study, propose, and promote the use of endemic plants in nanomaterial synthesis processes. On the other hand, the applications of the Fe_3O_4 nanoparticles in the field of degradation of organic pollutants and environmental remediation has been extensively studied due to their photocatalytic properties and the emerging need for environmental remediation [32–35]. In this work, we report an environmentally friendly alternative synthesis route of Fe_3O_4 nanoparticles with significant antibacterial and photocatalytic activity evaluated in Congo red (CR) degradation. A kinetic absorption model was conducted to describe in detail the CR degradation process.

2. Materials and Methods

2.1. Bio-Synthesis of Fe_3O_4 Nanoparticles

The synthesis of the particles was carried out from a precursor solution consisting of ferric chloride ($\text{FeCl}_3 \cdot 6\text{H}_2\text{O}$) and ferrous chloride ($\text{FeCl}_2 \cdot 4\text{H}_2\text{O}$) in a 2:1 molar ratio. The Fe^{2+} and the Fe^{3+} ions were reduced using *Cnicus benedictus* extract. Briefly, the *Cnicus benedictus* extract was obtained, dried, and milled with 3.87 g of *Cnicus benedictus* leaves, then it was mixed with 80 mL of deionized water. The mixture was heated to 150 °C for 15 min. After this time, the infusion obtained was filtered and transferred to the precursor solution of [Fe (III)/Fe (II)]. The pH of the mixture was adjusted to 12 by an NaOH solution. After 20 min of magnetically stirring, the reduction of Fe ions was carried out. A color change of the post-reaction solution from dark reddish color into black color was observed. This coloration change suggested the formation of the Fe_3O_4 nanoparticles (Figure 1).

2.2. Materials CHARACTERIZATION

The size distribution and the morphology were identified using high-resolution scanning electron microscope (HR-SEM) brand Hitachi SU8230 cold field emission at 3.0 keV. The elemental mapping by energy dispersive X-ray spectroscopy (EDS) was performed by a Bruker XFlash 6/60 system coupled to the microscope. The X-ray diffraction (XRD) analysis was carried out through an X-ray diffractometer (Rigaku Ultima IV), with Cu K α radiation ($\lambda = 1.5406 \text{ \AA}$) at a scan rate of 0.05°/step with a speed of 2°/min in a diffraction range of 30–80° at room temperature using parallel-beam geometry. Raman spectroscopy of the sample was performed in solid state using a dispersive Raman spectrometer (Bruker-Senterra) equipped with a microscope and a laser with $\lambda = 785 \text{ nm}$ in a range from 200 to 800 cm^{-1} .

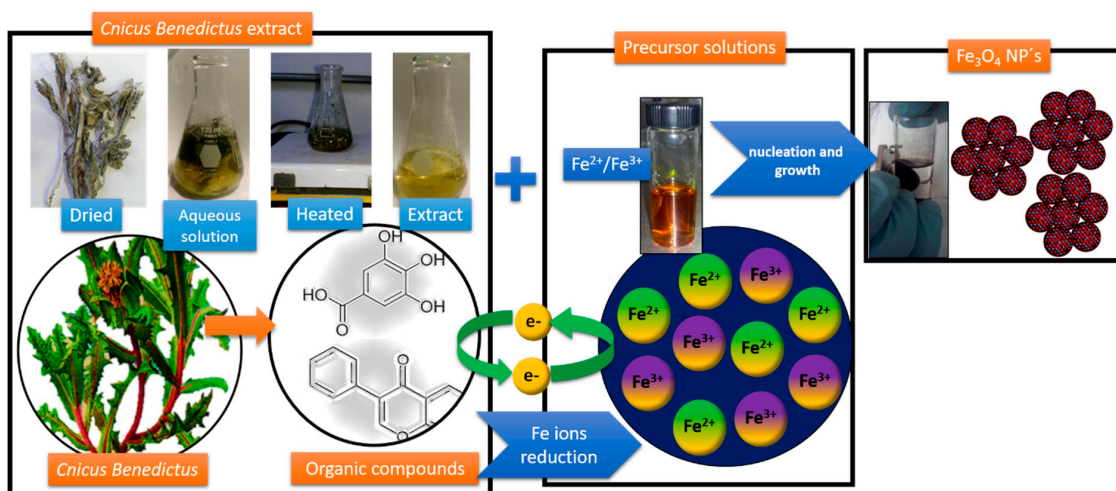


Figure 1. Schematic representation of the green procedure to obtaining Fe₃O₄ NPs by *Cnicus benedictus* as reducing agent.

2.3. Congo Red Photo Degradation

The photocatalytic activity assay of Fe₃O₄ nanoparticles was carried out through the degradation of CR. The experiments were performed using 1 mL of organic dye (CR) employed at 4 ppm. Posteriorly, Fe₃O₄ NPs synthesized by *Cnicus benedictus* were added to the CR solution. The concentration of Fe₃O₄ NPs was 20 µg/mL. The CR photodegradation process was monitored by Uv-vis equipment (Metash UV6000) in a range of 200–800 nm and a step of 2 nm with a bandwidth of 1.8 nm, ±0.5 nm of wavelength accuracy, and 0.3 nm of wavelength repeatability in intervals of 3 min until the SPR of the CR disappeared. In order to discard an intrinsic photobleaching associated with Congo red, a control experiment with CR and in the absence Fe₃O₄ NPs was carried out. The photodegradation of the CR was evaluated for a period of 40 min, and no variations were observed in the characteristic absorbance of the Congo red.

2.4. Antibacterial Activity

The antibacterial effect was tested with the Kirby-Bauer method. The Gram-positive *Staphylococcus aureus* (*S. aureus*) and Gram-negative *Escherichia coli* (*E. coli*) bacteria were employed to determine the antimicrobial behavior of the Fe₃O₄ NPs. The microbial cultures were incubated at 36 °C for 24 h. Solutions of Fe₃O₄ NPs were put in contact with studied bacteria. Six filter paper discs of 5 mm of diameter were impregnated with 5 mL of Fe₃O₄ NPs. Solutions of iron nanoparticles at different concentrations were performed and labeled. Specifically, C1 was associated with the disk control, and the samples labeled as C2 (5 mM), C3 (10 mM), C4 (15 mM), C5 (20 mM), and C6 (25 mM) corresponded to the different Fe₃O₄ NPs concentrations. Finally, the measurements of the inhibition zone were collected. Statistically, an ANOVA analysis was employed to validate the measurement of the inhibition zone and, consequently, the antibacterial effect of the Fe₃O₄ NPs. The comparison between the antibacterial behavior of *E. coli* and *S. aureus* was modeled mathematically by curve fit models.

3. Results and Discussion

3.1. Scanning Electron Microscopy

The Fe₃O₄ NPs were characterized by scanning electron microscopy (SEM). Figure 2a shows a secondary electrons image obtained at 15 kV; in this image, it is possible to identify the morphology and the distribution size of the Fe₃O₄ NPs synthesized by *Cnicus benedictus*. The Fe₃O₄ NPs show agglomeration due to the steric effect of the nanoparticles [20]. However, in Figure 2b, the individual

nanoparticles confined in a cluster were observed. The average distribution size of the nanoparticles was 20 nm approximately. This value could be considered as a first approximation. Subsequent analysis by XRD supported this fact. Additionally, an EDS mapping of the sample is presented in Figure 2c, which displays the Fe and the O as constitutive elements of the sample. In this sense, it was possible to affirm that the Fe_3O_4 NPs could be synthesized by *Cnicus benedictus* as the reducing agent, thus offering a new alternative in the green chemical in the field of synthesis of iron oxides nanoparticles Fe_3O_4 NPs. Nevertheless, a more precise characterization of the iron oxides obtained was necessary and is presented below.

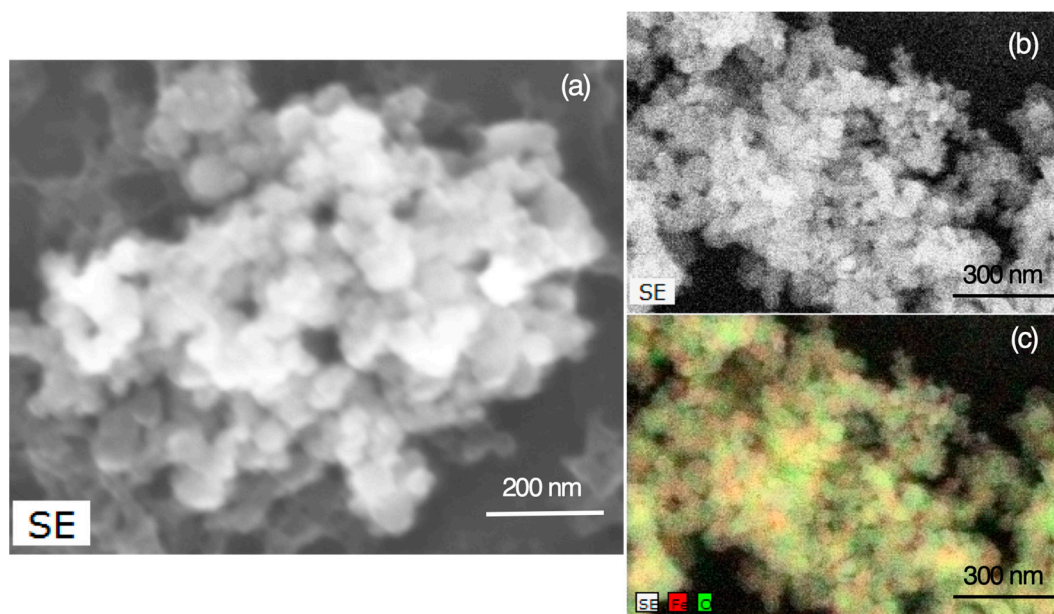


Figure 2. SEM image obtained by secondary electrons at (a) 130, (b) 80 kx, and (c) EDS mapping of Fe_3O_4 NPs obtained by *Cnicus benedictus*.

3.2. X-Ray Analysis of the Nano-Crystalline Fe_3O_4

Figure 3a shows the experimental X-Ray diffraction pattern associated with the sample synthesized by the green route using *Cnicus benedictus*. Based on the diffraction peaks observed in the experimental XRD pattern, it was possible to correlate this XRD pattern with the cubic structure (Fm3m-325) of the magnetite (JCPDF# 96-900-5813). In order to support the structural characterization of the sample, Table 1 indicates the location of the diffraction peaks (2θ), the interplanar distance (d-spacing), and the hkl index typical of the magnetite structure.

Table 1. Parameters obtained from the XRD patterns of the Fe_3O_4 NPs and involved in the Williamson-Hall analysis. FWHM: full width at half maximum.

2θ	d-spacing	hkl	FWHM (Corrected)	Asymmetry	Areal Asymmetry	Integral Breadth	Shape Factor	Size Uncorrected	Size Corrected
30.24	2.9571	220	0.5069	1.0005	1.6403	0.588	0.861	18.03811703	18.3
35.62	2.5185	311	0.6984	0.7643	0.7378	0.893	0.782	13.27506532	13.4
38.1	2.4213	222	0.4058	0.6814	0.8878	0.242	1.68	23.01235689	24.1
43.2	2.0925	400	0.8135	1.4181	1.2442	0.277	2.936	11.67014924	11.8
53.62	1.7061	422	0.46792	1.1632	1.0717	0.3921	1.052	21.13618779	21.1
57.08	1.6102	511	0.7651	1.7009	1.1468	0.486	1.576	13.13289818	13.5
62.84	1.4802	440	0.6574	0.8412	0.994	0.646	1.017	15.73424925	16.6

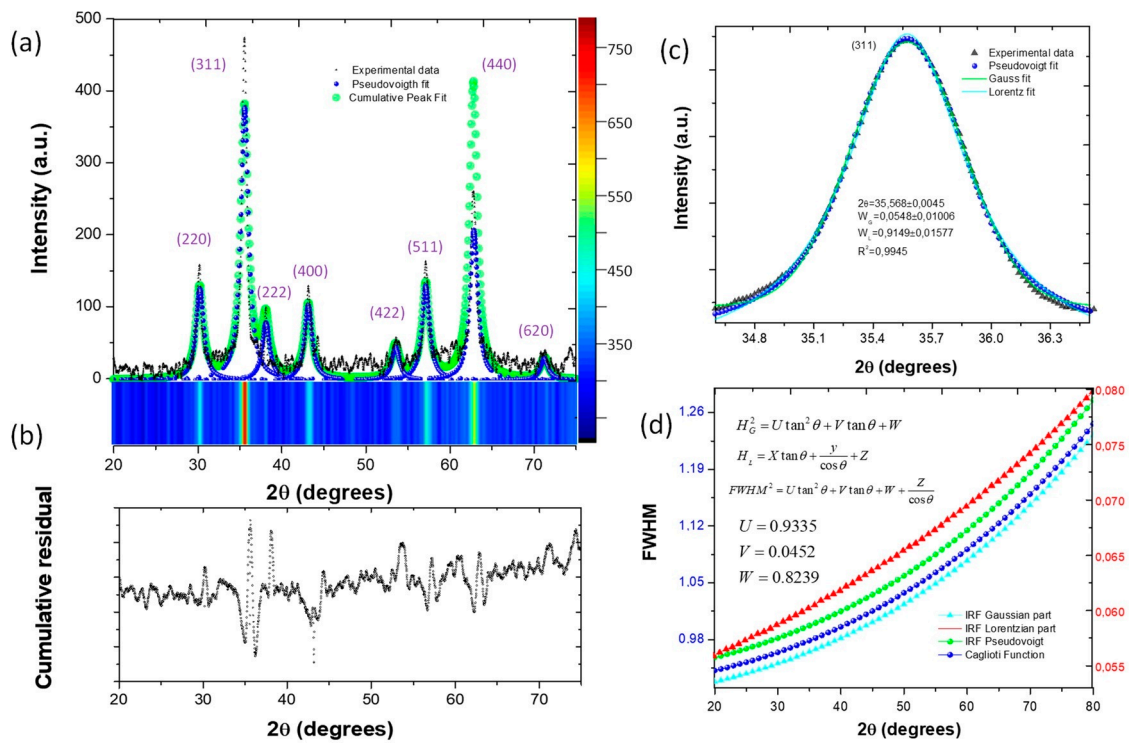


Figure 3. (a) XRD pattern profile fitting and pseudo-Voigt analysis of broadening. (b) Cumulative residual fitting peak (c) Fitting intensity of the (311) plane of the magnetite and (d) convolution of the instrumental resolution function (IRF)

On the other hand, the crystallite size and strain could be calculated from the experimental XRD pattern according to the Williamson-Hall method. However, in the first part of the Williamson-Hall analysis, it was necessary to obtain parameters derivate to the fit of the peaks profile.

The diffraction profile from the Fe_3O_4 nanoparticles was fitted with pseudo-Voigt (pV) function [36–38]. The pseudo-Voigt function is the convolution of Gauss and Lorentz functions. In general form, pV function is given by [39]:

$$pV(x) = \eta G(x) + (1 - \eta)L(x) \quad (1)$$

where $G(x)$ and $L(x)$ are defined as the sum of the Gaussian peak and the Lorentzian peak, respectively. In both functions, parameters such as height (height of the peak at the maximum) peak center (position of the maximum) and FWHM (full width at half maximum of the peak) are involved. In this sense, it is necessary to obtain the normalized peaks of Gauss ($G'(x)$) and Lorentz ($L'(x)$), consequently, the $pV(x)$ can be expressed as:

$$pV(x) = I[\eta G'(x, \Gamma) + (1 - \eta)L'(x)] \quad (2)$$

where I is the intensity of the peak normalized by Gauss and Lorentz. Γ is the FWHM for Gaussian and Lorentzian peaks, x_0 is the peak position, and η is the Gaussian ratio. The Lorentzian part is described by:

$$L(x) = \frac{1}{\pi} \frac{\Gamma/2}{(x - x_0)^2 + (\Gamma/2)^2} \quad (3)$$

and the Gaussian part is:

$$G(x) = \frac{1}{\sigma \sqrt{2\pi}} e^{-\frac{(x-x_0)^2}{2\sigma^2}} \quad (4)$$

Finally, the pseudo-Voigt expression was employed for the fit profile peaks in the XRD analysis of the Fe₃O₄ nanoparticles and can be written as follows [40]:

$$pV(x) = h * [\eta * \exp\left(-\frac{(x-x_0)^2}{2\sigma^2}\right) + (1-\eta) \frac{(\Gamma/2)^2}{(x-x_0)^2 + (\Gamma/2)^2}] \quad (5)$$

where:

$$h = \frac{2I}{\pi\Gamma} [1 + (\sqrt{\ln 2} - 1)] \quad (6)$$

$$\sigma = \frac{\Gamma}{2\sqrt{2\ln 2}} \quad (7)$$

In this sense, Figure 3a,b, show the multi-peaks fitting analysis and the cumulative residual fitting peak associated with the residual fit in the analysis, respectively.

In representative form of the fitting peaks, Figure 2c illustrates the fitting intensity associated with the (311) plane of the magnetite; in this plot, it is possible to observe the Gaussian and the Lorentzian parts corresponding to the Pseudo-Voigt fit process. In this case, a correlation factor (R^2) of 0.9945 was observed. Consequently, this result indicated that the FWHM values were consistent for the subsequent analysis. In order to support the pseudo-Voigt profile peak fitting, the instrumental resolution function (IRF) of the equipment is described in Figure 3d. The IRF was plotted from the modified Caglioti equation, which is described as follows [38]:

$$FWHM^2 = U \tan^2 \theta + V \tan \theta + W + \frac{Z}{\cos \theta} \quad (8)$$

Additionally, the IRF was calculated by the pseudo-Voigt method. In this procedure, the Gaussian (HG) and the Lorentzian (HL) parts were calculated started from the following expressions [39]:

$$H_G^2 = U \tan^2 \theta + V \tan \theta + W \quad (9)$$

$$H_L = X \tan \theta + \frac{Y}{\cos \theta} + Z \quad (10)$$

The HG and the HL parts of the IRF are shown in graph 3(d). The convolution of the HG and the HL is presented in the IRF pseudo-Voigt (HpV) graph (Figure 3d). It is important to note that the HpV and the Caglioti curve are very similar due to the refinement of U, V, and W parameters.

3.3. Williamson-Hall Analysis

Based on the results obtained from the pseudo-Voigt analysis, the FWHM values were employed to calculate the crystallite size and strain, which could be obtained by the Williamson-Hall plot method. This method presupposes that the peaks observed from the X-ray diffraction pattern are the convolution of the Gaussian part (broadening due to the strain) and the Lorentzian part (influence of the crystallite size) [6,39,41] Mathematically, this relationship can be expressed in the reciprocal space as:

$$\frac{\beta \cos \theta}{\lambda} = \frac{1}{D_V} + 2\varepsilon \left(\frac{2 \sin \theta}{\lambda} \right) \quad (11)$$

In this sense, from the graph of the $(\beta \cos \theta)$ versus $(2 \sin \theta / \lambda)$, it is possible to obtain the microstrain and the domain size with the values of slope and intercepts, respectively.

The Williamson-Hall plot is described in Figure 4a. In this case, the crystallite size obtained by the pseudo-Voigt method was 17.47 nm. In order to corroborate this value, Table 1 describes the parameter involved in the Williamson-Hall plot analysis. The profile function employed in the calculations was the pseudo-Voigt model. However, the values of the Gauss and the Lorentz parts were compared and

are shown in Figure 4b,c, respectively. In all cases of the profile-fitting analysis of XRD peaks, similar values of crystallite size were obtained.

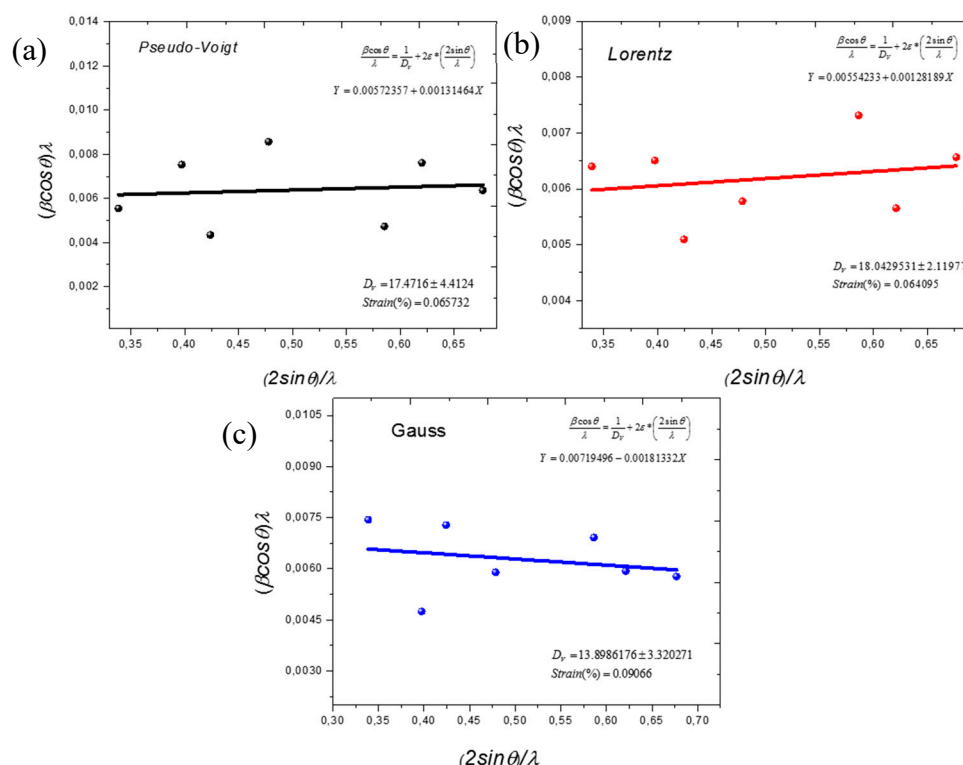


Figure 4. Williamson-Hall plot of the Fe_3O_4 NPs synthesized by *Cnicus benedictus* calculated by the (a) Pseudo-Voigt, (b) Lorentz and (c) Gauss functions.

Table 2 shows the values of the crystallite size and strain calculated for the sample. The calculations performed based on the FWHM of each intensity show a stable size and strain associated with the sample. In this case, the crystallite size was 14 nm according to the size observed by SEM. It is important to note that the pseudo-Voigt method is a functional and highly accurate method for calculating the crystallite size from the XRD patterns; due to this method, it is a combination of the Lorentz and the Gauss method for fit peak profiles, which makes it an excellent tool for XRD pattern processing [38].

Table 2. Crystallite size and strain calculated from pseudo-Voigt, Lorentz, and Gauss methods.

Profile Function	Profile Broadening	Size (nm)	Strain (%)
Pseudo-Voigt	FWHM	14.45 ± 6.27	0.289 ± 0.145
	Integral breadth	18.10 ± 4.32	0.1624 ± 0.192
Lorentzian	FWHM	18.04 ± 2.11	0.0640 ± 0.017
	Integral breadth	22.11 ± 4.98	0.032 ± 0.016
Gaussian	FWHM	13.89 ± 3.32	0.09 ± 0.181
	Integral breadth	17.70 ± 5.78	0.012 ± 0.154

3.4. Raman Spectroscopy

In order to elucidate the oxidative phases obtained from the green synthesis of the nanoparticles, a Raman analysis is presented in Figure 5. In this figure, it is possible to identify three phases associated with the iron oxide. The main phase identified was magnetite with an approximate value of 45.5%, and the second phase was hematite (39.81%), and the minority phase was maghemite (Table 3). These results can be attributed to the facile oxidation of the NPs due to the interaction with the medium.

However, it is important to mention that the XRD analysis supported the formation of Fe_3O_4 as the main phase. However, the reduction of the Fe ions by *Cnicus benedictus* was carried out as a result of the synthesis of Fe_3O_4 . It has been reported that the presence of antioxidants in some organic extracts promotes Fe ions reduction [42]. Specifically, the *Cnicus benedictus* extract offers a green alternative to obtain Fe_3O_4 NPs.

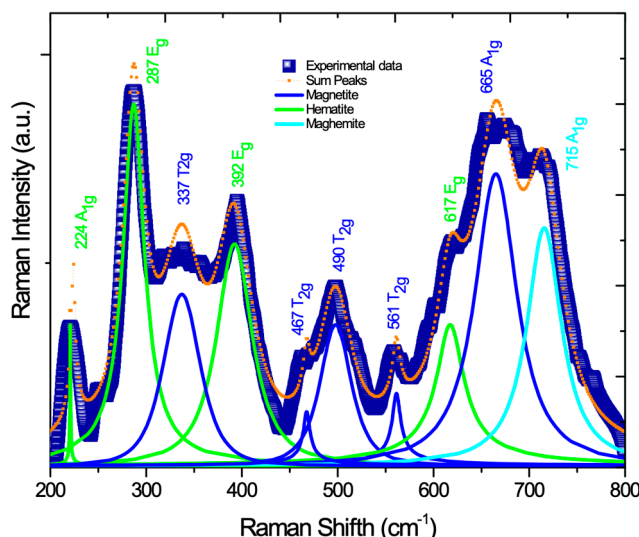


Figure 5. Deconvolution analysis of the Raman spectra of Fe_3O_4 NPs.

Table 3. Deconvolution of Raman spectra for the quantification of iron oxide phases obtained by green synthesis route.

Phase	Center Max	Phonon Modes	Max Height	FWHM	Area	% Phase
Magnetite	337.223	T_{2g}	205.855	454.371	1145.410	8.82417337
	467.565	T_{2g}	649.779	100.823	470.199	3.6223863
	490.854	T_{2g}	169.265	389.238	845.322	6.51231252
	561.327	T_{2g}	868.329	127.992	818.774	6.30778824
	665.161	A_{1g}	350.471	524.393	2627.970	20.2457311
						45.5123916
Hematite	224.171	A_{1g}	193.966	615.686	908.971	7.00266079
	287.060	E_g	434.132	275.124	1047.700	8.0714211
	392.236	E_g	266.167	444.447	1656.890	12.7645861
	617.429	E_g	169.405	38.060	1554.730	11.9775513
						39.8162194
Maghemite	715.584	A_{1g}	285.457	43.956	1904.400	14.6713891

Table 3 describes the location of the main intensities observed in the Raman spectra of the Fe_3O_4 NPs synthesized by environmentally friendly methodology. Moreover, the phonon modes attributed to each intensity are shown in Table 3. These values are supported by previous studies reported in the literature [43–45]. This result is conclusive in respect to the iron oxide obtained by the green synthesis method, although with *Cnicus benedictus*, we can affirm that it is possible to obtain Fe_3O_4 NPs in the majority phase and consequently evaluate the magnetic and the catalytic properties of the magnetite.

3.5. Analysis of Magnetic Properties of the Fe_3O_4 Obtained by Green Route

Figure 6 shows the hysteresis curve or the magnetization curve of the Fe_3O_4 NPs. In this figure, we can observe an approximately superparamagnetic behavior [38,46,47]. The saturation magnetization (Ms) value was 43.85 emu/g, while the coercivity field (Hc) of the sample was 143.75 Oe. Both values

were consistent with the typical values reported in the literature for superparamagnetic materials [48,49]. In this sense, it was possible to affirm that the sample of Fe_3O_4 NPs effectively had a superparamagnetic behavior and, consequently, their potentials application in optoelectronics or biomedicine, among others, is notable. In other words, the green synthesis of Fe_3O_4 NPs by *Cnicus benedictus* offers an environmentally friendly alternative for obtaining magnetic nanoparticles.

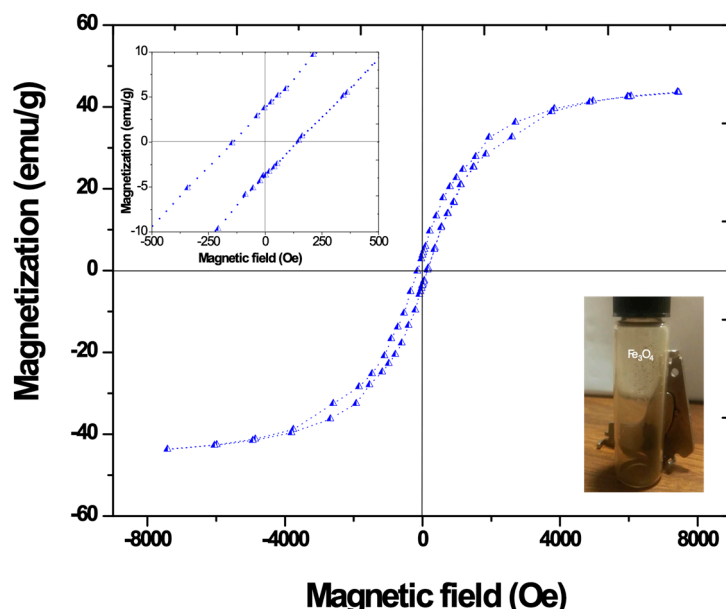


Figure 6. Magnetic hysteresis loop of the Fe_3O_4 NPs at room temperature.

3.6. Photocatalytic Effect: Congo Red (CR) Degradation

In order to evaluate the photocatalytic behavior of the Fe_3O_4 NPs, a CR degradation process was conducted. Figure 7a shows the UV-vis spectra associated with the CR Fe_3O_4 NPs and the CR Fe_3O_4 samples at an initial time ($t = 0$). In this figure, the characteristic peak associated with the CR was observed at 500 nm in the samples of CR and Fe_3O_4 /CR. Figure 7b illustrates the CR degradation process, in which it was possible to observe the CR degradation in a reaction time of 36 min. This fact indicated that the CR degradation by Fe_3O_4 NPs was possible due to the reactivity of the nanoparticles obtained by green synthesis route.

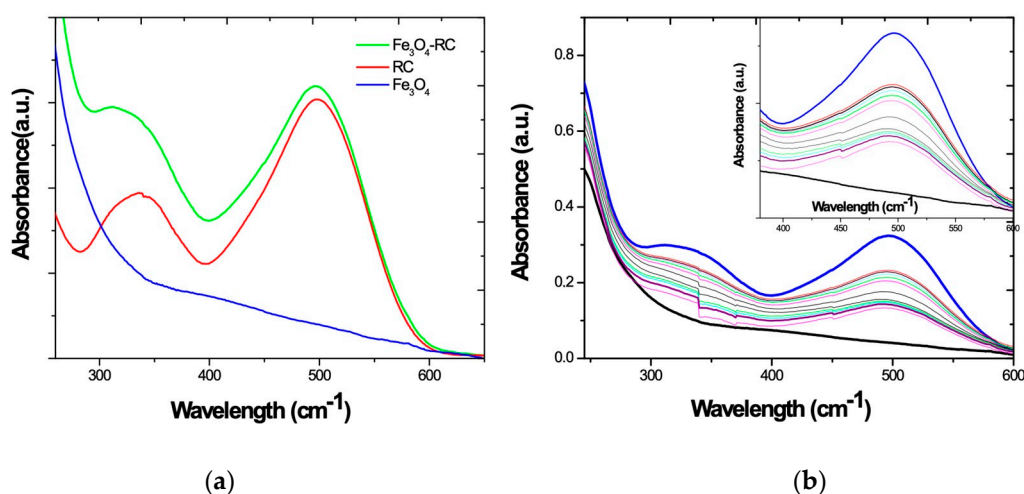


Figure 7. UV-vis spectra of the (a) Fe_3O_4 NPs, the Fe_3O_4 NPs-CR, and the CR (40 mgL^{-1}) and (b) Congo red photodegradation by Fe_3O_4 NPs synthesized using *Cnicus benedictus*.

In general form, this behavior can be explained as a combination of oxidation and reduction processes in which the surface of the Fe_3O_4 NPs is a substrate where the CR molecules are absorbed. Subsequently, the nanoparticles act as active sites for the electron interactions between the organic dyes and the Fe_3O_4 NPs. The photocatalytic mechanism for organic dyes degradation involves the dye excitation under visible light with wavelength ($\lambda > 400\text{nm}$) from the ground state (Dye^0) to the triplet excited state (Dye^*). During this procedure, the excited state dye species generates a semi-oxidized radical cation ($\text{Dye}^{\bullet+}$) by an electron injection into the conduction band of Fe_3O_4 . A derivate to the reaction between the trapped electrons and the dissolved oxygen in the system with superoxide radical anions ($\text{O}_2^{\bullet-}$) are generated [50,51]. Consequently, this superoxide radicals anion results in hydroxyl radicals (OH^\bullet) formation [52–54], which are responsible for the oxidation and the degradation of the organic dye compound present in the CR (Figure 8).

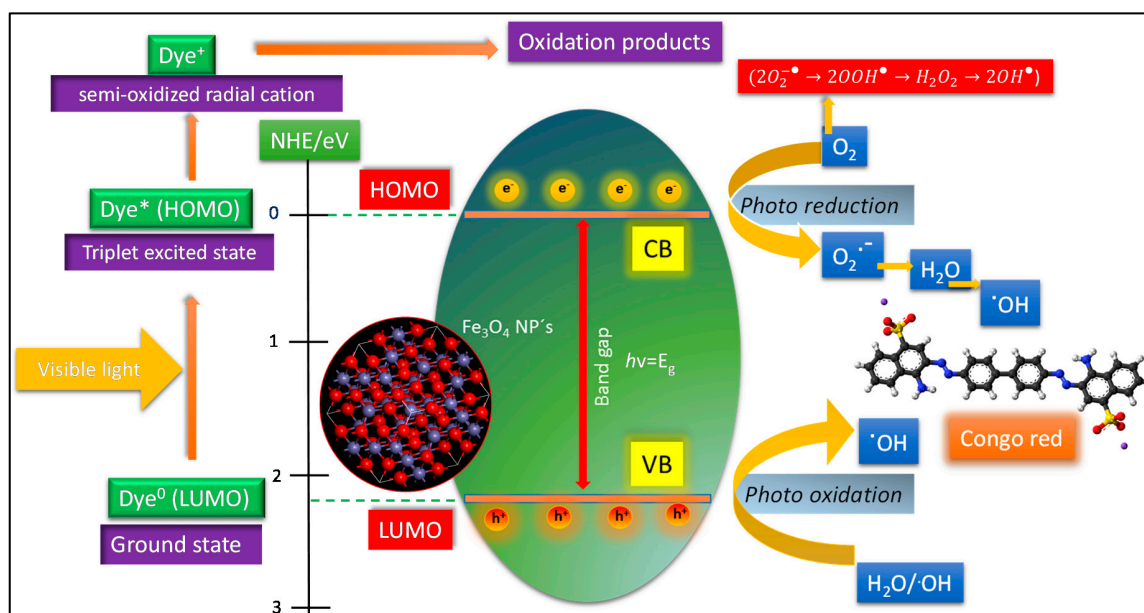


Figure 8. Schematic representation of dye photodegradation process.

On the other hand, the adsorption rate and the equilibrium concentration at which CR is degraded can be described in detail by theoretical adsorption models.

3.7. Theoretical Adsorption Kinetic Models

In order to describe the adsorption kinetic behavior of the Fe_3O_4 NPs, four theoretical models were analyzed with respect to the experimental data obtained from the photodegradation of the CR by Fe_3O_4 NPs. Pseudo-first order, Pseudo-second order, Elovich, and Intraparticle diffusion models were employed to describe and calculate the kinetics adsorption parameters of the organic dye. The equations that govern these models are described in Table 4, and which have been described in several reports [6,35,42,55].

Table 4. Theoretical adsorption models employed for the photodegradation of the CR by Fe_3O_4 NPs.

Theoretical Model	Equation
Pseudo first order	$\frac{dq}{dt} = K_1(q_e - q_t)$
Pseudo second order	$\frac{dq}{dt} = K_2(q_e - q_t)^2$
Elovich	$\frac{dq_t}{dt} = \alpha e^{-\beta q_t}$
Intraparticle diffusion	$q_t = k_i \sqrt{t} + C_i$

Figure 9a–d show the graphs associated with theoretical kinetic adsorption models. The correlation values existent between the experimental data and the theoretical model are described in Table 3. In this table, it is possible to observe that the intraparticle diffusion model exhibited the highest correlation value R^2 , (0.9557). Based on this result, we could affirm that the CR degradation process was carried out in addition to the intraparticle diffusion process. From the physic-chemical point of view, the intraparticle diffusion model was described by three steps. Firstly, an instantaneous adsorption was detected because the concentration in the external solution was sufficiently high. Then, a gradual adoption was observed during the CR degradation process. The time associated with this step depended on the system variables such as temperature, absorbent particle size, and solute concentration [56–59]. Finally, the organic molecules that degraded exhibited a slow adsorption rate until the final equilibrium. Therefore, the intraparticle diffusion model can describe the CR degradation process and the solute concentration, and the particle size of the Fe_3O_4 NPs takes a preponderant role in the CR degradation rate.

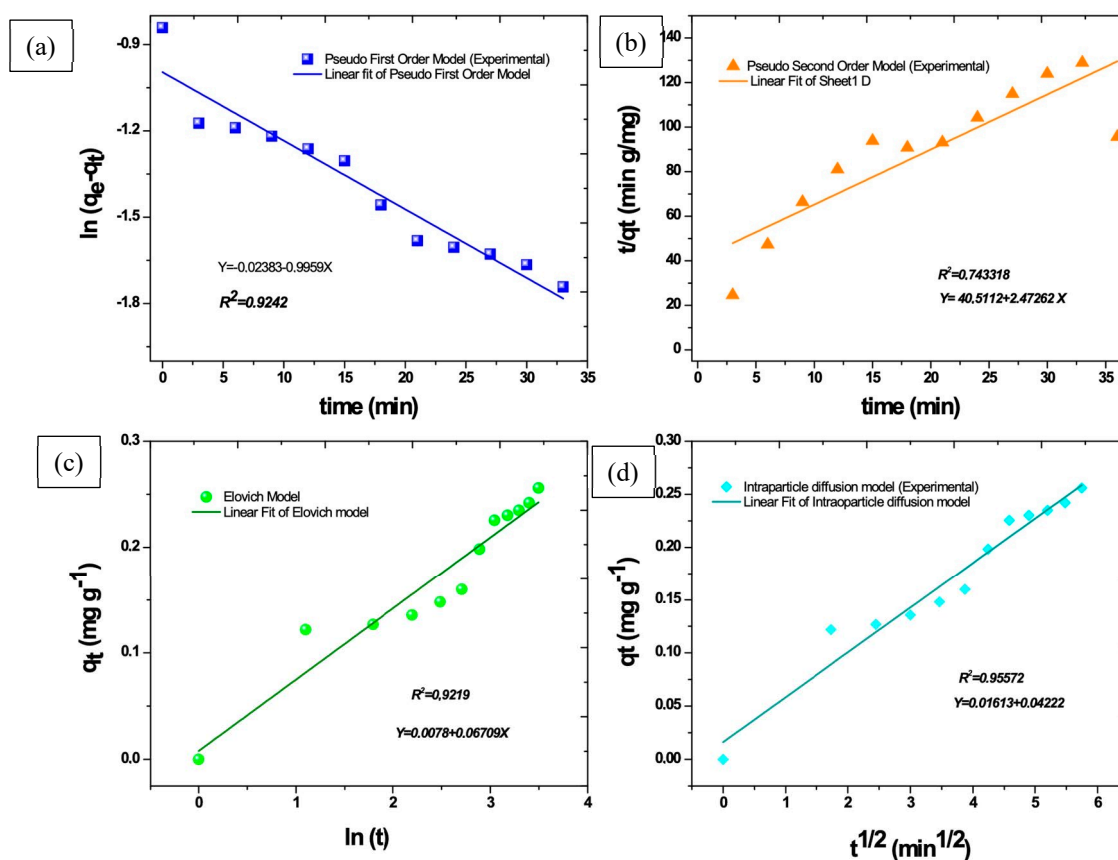


Figure 9. Experimental and theoretical kinetic adsorption models: (a) Pseudo-first order, (b) Pseudo-second order, (c) Elovich, and (d) Intraparticle diffusion models.

3.8. Antibacterial Effect

In order to evaluate the antibacterial effect of the Fe_3O_4 NPs obtained by green route, the inhibition zones in *E. coli* and *S. aureus* bacteria strains were measured. Figure 10a displays the inhibition zones presented by the Fe_3O_4 NPs at different Fe_3O_4 NPs concentrations. In this plot, the antibacterial effect was major in the case of the *E. Coli* bacteria in comparison to the *S. aureus* strain. Moreover, the differences between the variances of inhibition zones were determined by an ANOVA analysis. In this process, the p -value corresponding to the F-statistic was lower than 0.05 ($p < 0.05$), this value suggesting that one or more treatment was significantly different. It was possible to affirm that the Fe_3O_4 NPs obtained by *Cnicus Benedictus* had an antibacterial effect due to the box-plot of the ANOVA analysis (Figure 10b)

showing significant differences in relation to the control sample. In this case, C1 was associated with the disk control, and the samples labeled as C2 (5 mM), C3 (10 mM), C4 (15 mM), C5 (20 mM), and C6 (25 mM) corresponded to the Fe_3O_4 NPs concentrations. On the other hand, post hoc Tukey HSD test could be employed to identify which pairs of treatments were significantly different from each other. Figure 10c illustrates graphically the Tukey test and the pairs of treatments with significant differences (inset Figure 10c). Through these results, the bactericidal effect of nanoparticles could be statistically corroborated. It was verified that this effect is related to the capacity of the particles to interact with the bacterial membrane, generating structural and physiological changes in the microorganism and generating its elimination. It has been reported that the Fe_3O_4 NPs exhibit remarkable reactivity with phosphorus and sulfur compounds, which are present in the proteins of the cell membrane in the bacteria [60,61]. In others words, the electronegative groups of polysaccharides on the bacterial membrane can act as sites of attraction for Fe_3O_4 NPs and iron cations. This fact generates alterations in the structure and the permeability of the cell membrane due to the excess of metals or metallic ions that promote a disorder in metabolic functions [62]. In this sense, the difference between the antibacterial effects presented by *E. coli* and *S. aureus* can be attributed to the structural differences associated with Gram-positive and Gram-negative bacteria and their cell membranes. In the case of the *S. Aureus*, the cell membrane was smooth and single-layered and the thickness of the cell wall was 20–80 nanometers, while the *E. Coli* bacteria had a wavy and double-layered cell wall, but the thickness of the cell wall was minor in comparison with the Gram-positive bacteria. In this sense, the major antibacterial effect observed in the *E. coli* bacteria could be explained as a function of their cellular structure and cell wall morphology [25].

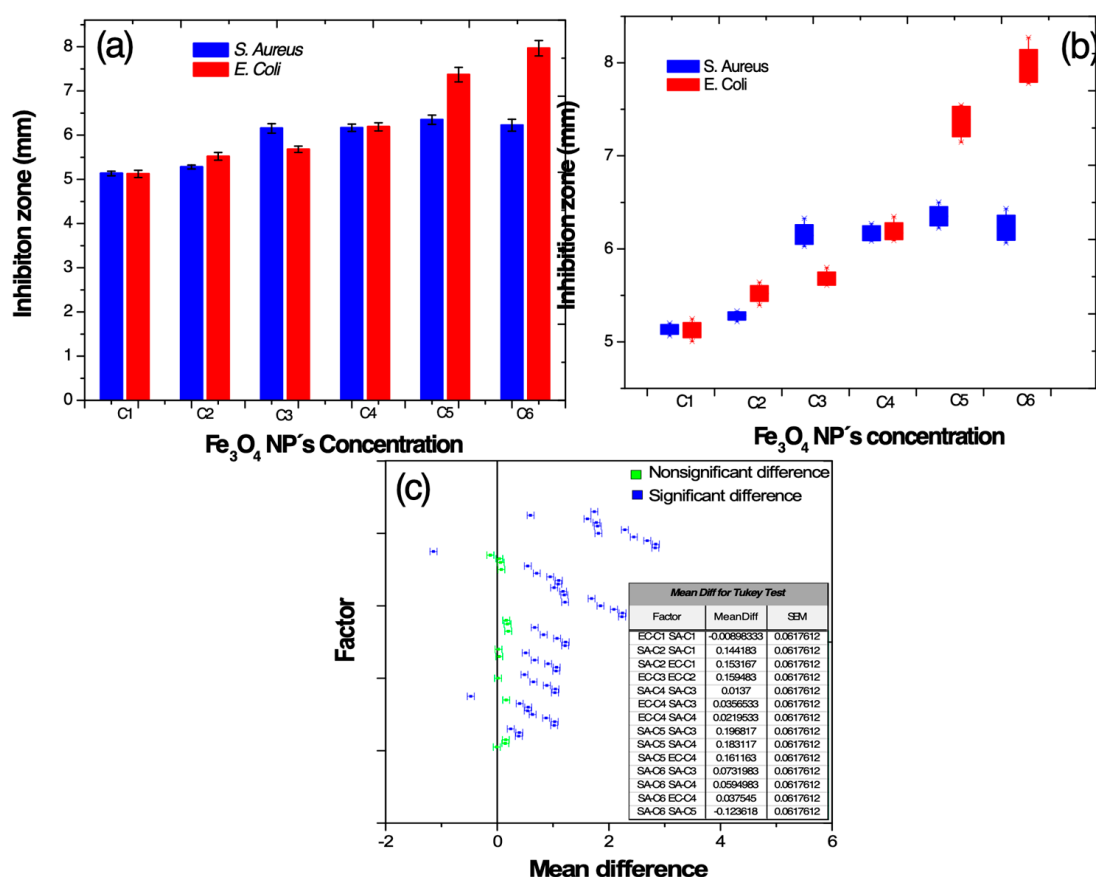


Figure 10. (a) Bar graphs of the diameter of the inhibition zone measured from the bacterial susceptibility, (b) box-plot of antibacterial activity of Fe_3O_4 against *S. aureus* and *E. coli* bacteria. (c) Scatter plot of Tukey comparison by pairs.

Finally, based on the experimental data corresponding to antibacterial behavior of the Fe_3O_4 NPs, it could be modeled mathematically. Starting with graph 11(a), which describes the antibacterial response of *E. Coli* and *S. Aureus* bacteria to the Fe_3O_4 NPs, it was possible to associate this behavior with the sigmoid dose-response curve model fit, which is described by the following equation:

$$y = A_1 + \frac{A_1 - A_2}{1 + 10^{(\log x_0 - x)p}} \quad (12)$$

Figure 11b models graphically the antibacterial response of the *S. aureus* bacteria to the Fe_3O_4 NPs synthesized by *Cnicus benedictus* and their corresponding parameters. It is important to note that the correlation factor R^2 was 0.98. Thus, the dose response fitting could describe, with high precision, the experimental bactericidal behavior of the *S. aureus*.

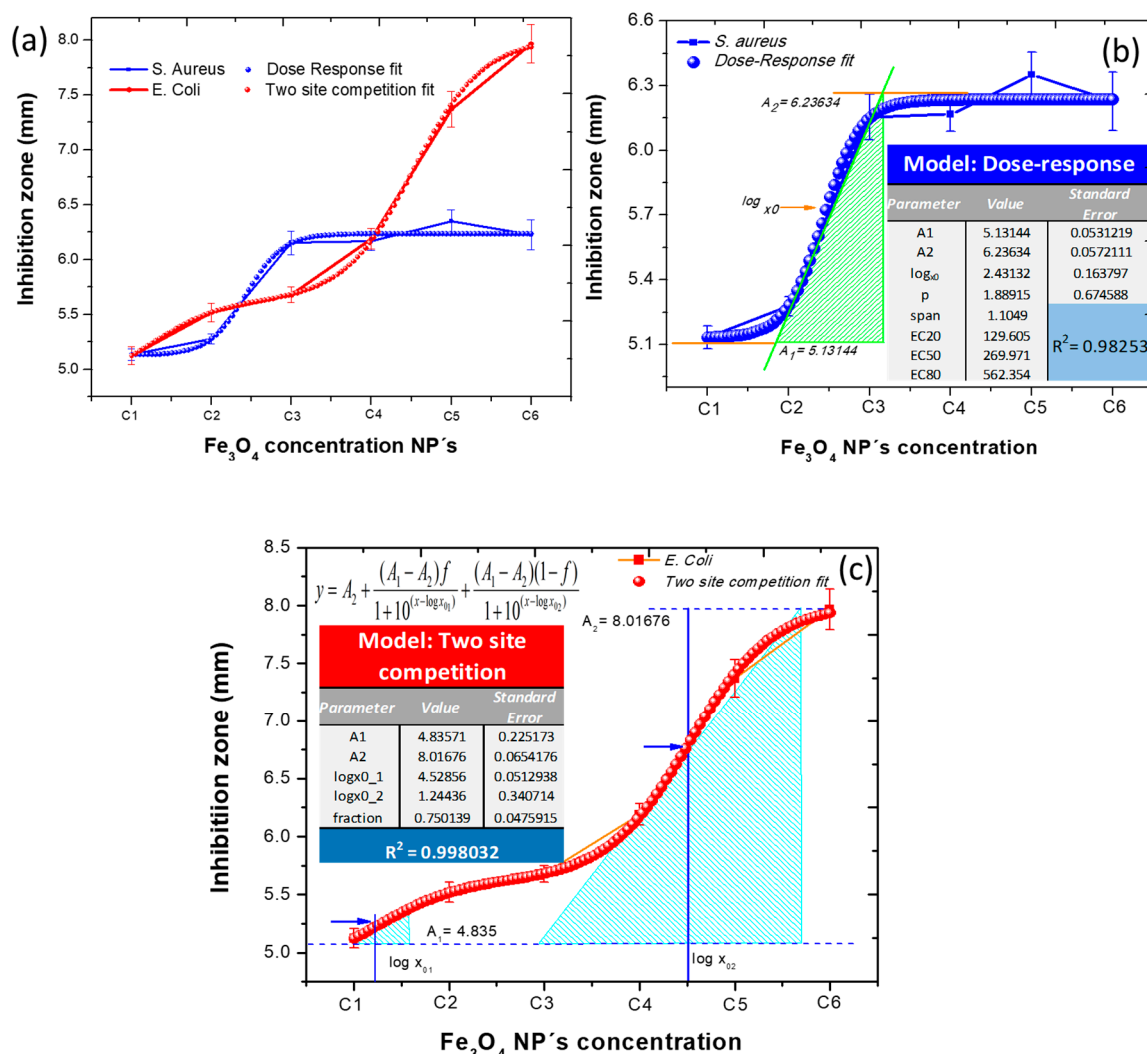


Figure 11. Antibacterial curve fitting (a) comparison between *E. coli* and *S. aureus*. (b) *S. aureus* behavior (dose response model) and (c) *E. coli* behavior (two sites competition model).

On the other hand, the bactericidal effect of the Fe_3O_4 NPs against *E. coli* also was modeled mathematically. However, the best fit of the experimental data associated with the Gram-negative bacteria (*E. coli*) was fit to the two sites competition model, which is described by:

$$y = A_2 + \frac{A_1 - A_2}{1 + 10^{(x - \log x_{01})}} + \frac{A_1 - A_2(1 - f)}{1 + 10^{(x - \log x_{02})}} \quad (13)$$

In this case, the R^2 value was 0.998, and the associated parameters are inset in the Figure 11c. Consequently, by the two sites, the competition model could describe the bactericidal behavior of the Fe_3O_4 NPs against *E. Coli* bacteria. This fact indicated that the two site competition models attributed to the antibacterial effect against *E. coli* were more complex in comparison to the *S. aureus* behavior. However, this effect was significantly notable. This fact supports the discussion in regard to the characteristics of the Gram-positive and the Gram-negative bacteria described previously; the thickness of the cell wall of the bacteria has a preponderant role in the antibacterial behavior.

In conclusive form, it was possible to affirm that the Gram-negative bacteria (*E. Coli*) was more susceptible to the interaction with the Fe_3O_4 NPs, which exhibited high specific surface area, promoting better contact with the microorganisms; consequently, the Fe_3O_4 NPs could be attached to the cell membrane and penetrate inside the bacteria.

4. Conclusions

The green synthesis by *Cnicus benedictus* as a reducing agent offers an environmental friendly alternative to obtaining Fe_3O_4 NPs. The organic compounds present in the *Cnicus benedictus* extract have the capacity to carry out the iron ions reduction and, consequently, the Fe_3O_4 NPs formation in the majority phase. Iron oxides such as hematite and maghemite were also observed in our study. However, the mentioned iron oxide appeared in the minor phase due to the great reactivity of the iron oxides with the aqueous media promoting the facile oxidation of the iron oxide species. On the other hand, the obtained Fe_3O_4 NPs showed a very similar behavior to the superparamagnetic materials. This fact indicated that the nanoparticles synthesized can be evaluated for potential application in the magnetism materials field, among others. Additionally, this research was focused on environmental remediation applications, specifically in the Congo red photodegradation. Conclusively, it was observed that the Fe_3O_4 NPs are capable of carrying out the photodegradation of the organic dye (CR). Finally, it was possible to affirm that the Fe_3O_4 NPs synthesized by green route offer a facile, low cost, non-toxic, and environmental friendly alternative to obtaining functional Fe_3O_4 NPs with proven magnetic and catalytic properties. Additionally, it was possible to affirm that the Fe_3O_4 NPs exhibited an antibacterial effect. However, the Gram-negative bacteria (*S. aureus*) was more susceptible to the interaction with the Fe_3O_4 NPs, which exhibited high specific surface area, promoting better contact with the microorganisms and, consequently, the Fe_3O_4 NPs could be attached to the cell membrane and penetrate inside the bacteria.

Author Contributions: Conceptualization, formal analysis, investigation, writing—original draft preparation and project administration, Á.d.J.R.-B.; Investigation and review and editing, S.Y.R.-L.; methodology, D.L.-O.; investigation, data curation, N.M.-L.; investigation, review and editing, M.A.Z.A.; R.P.C., review and editing. All authors have read and agreed to the published version of the manuscript.

Funding: This research was funded by National Council for Science and Technology (CONACYT, México) in collaboration with the Center of Applied Physics and Advanced Technology (CFATA-UNAM) through “Cathedras CONACYT program”. Project number: 155.

Acknowledgments: Álvaro de Jesús Ruíz-Baltazar appreciates the support provided by the National Council for Science and Technology (CONACYT, México) in collaboration with the Center of Applied Physics and Advanced Technology (CFATA-UNAM) through “Cathedra CONACYT” program. Likewise, to the national materials characterization laboratory (LaNCaM) belonging to CFATA-UNAM.

Conflicts of Interest: The authors declare no conflict of interest for the publication of this work.

References

1. Ahmed, M.A.; Abou-Gamra, Z.M.; ALshakhanbeh, M.A.; Medien, H. Control synthesis of metallic gold nanoparticles homogeneously distributed on hexagonal ZnO nanoparticles for photocatalytic degradation of methylene blue dye. *Environ. Nanotechnol. Monit. Manag.* **2019**, *12*, 100217. [[CrossRef](#)]
2. Patwardhan, S.V.; Manning, J.R.H.; Chiacchia, M. Bioinspired synthesis as a potential green method for the preparation of nanomaterials: Opportunities and challenges. *Curr. Opin. Green Sustain. Chem.* **2018**, *12*, 110–116. [[CrossRef](#)]

3. Carabineiro, S.A.C. Supported Gold Nanoparticles as Catalysts for the Oxidation of Alcohols and Alkanes. *Front. Chem.* **2019**, *7*, 702. [[CrossRef](#)] [[PubMed](#)]
4. Argurio, P.; Fontananova, E.; Molinari, R.; Drioli, E. Photocatalytic membranes in photocatalytic membrane reactors. *Processes* **2018**, *6*, 162. [[CrossRef](#)]
5. Meramo-hurtado, S.I.; Zuurro, A. Environmental Assessment of Large Scale Production of Magnetite (Fe₃O₄) Nanoparticles via Coprecipitation. *Appl. Sci.* **2019**, *9*, 1682.
6. Jain, B.; Hashmi, A.; Sanwaria, S.; Singh, A.K.; Susan, M.A.B.H.; Carabineiro, S.A.C. Catalytic Properties of Graphene Oxide Synthesized by a “Green” Process for Efficient Abatement of Auramine-O Cationic Dye. *Anal. Chem. Lett.* **2020**, *10*, 21–32. [[CrossRef](#)]
7. Aghazadeh, M.; Karimzadeh, I.; Ganjali, M.R.; Mohebi Morad, M. A novel preparation method for surface coated superparamagnetic Fe₃O₄ nanoparticles with vitamin C and sucrose. *Mater. Lett.* **2017**, *196*, 392–395. [[CrossRef](#)]
8. Zhang, H.; Zhao, J.; Ou, X. Facile synthesis of Fe₃O₄ nanowires at low temperature (80 °C) without autoclaves and their electromagnetism performance. *Mater. Lett.* **2017**, *209*, 48–51. [[CrossRef](#)]
9. Hoseinpour, V.; Ghaemi, N. Green synthesis of manganese nanoparticles: Applications and future perspective—A review. *J. Photochem. Photobiol. B Biol.* **2018**, *189*, 234–243. [[CrossRef](#)]
10. Polo, A.M.S.; Lopez-Peñalver, J.J.; Sánchez-Polo, M.; Rivera-Utrilla, J.; López-Ramón, M.V.; Rozalén, M. Halide removal from water using silver doped magnetic-microparticles. *J. Environ. Manag.* **2020**, 253. [[CrossRef](#)]
11. Mi, S.; Liu, R.; Li, Y.; Xie, Y.; Chen, Z. Large low-field magnetoresistance of Fe₃O₄ nanocrystal at room temperature. *J. Magn. Magn. Mater.* **2017**, *428*, 235–238. [[CrossRef](#)]
12. Xu, J.; Li, Q.; Zong, W.; Zhang, Y.; Li, S. Ultra-wide detectable concentration range of GMR biosensors using Fe₃O₄ microspheres. *J. Magn. Magn. Mater.* **2016**, *417*, 25–29. [[CrossRef](#)]
13. Betancourt-Buitrago, L.A.; Hernandez-Ramirez, A.; Colina-Marquez, J.A.; Bustillo-Lecompte, C.F.; Rehmann, L.; Machuca-Martinez, F. Recent developments in the photocatalytic treatment of cyanide wastewater: An approach to remediation and recovery of metals. *Processes* **2019**, *7*, 225. [[CrossRef](#)]
14. Aguas, Y.; Hincapié, M.; Sánchez, C.; Botero, L.; Fernández-Ibañez, P. Photocatalytic inactivation of *Enterobacter cloacae* and *Escherichia coli* using titanium dioxide supported on two substrates. *Processes* **2018**, *6*, 137. [[CrossRef](#)]
15. Hernández-Abreu, A.B.; Álvarez-Torrellas, S.; Águeda, V.I.; Larriba, M.; Delgado, J.A.; Calvo, P.A.; García, J. Enhanced removal of the endocrine disruptor compound Bisphenol A by adsorption onto green-carbon materials. Effect of real effluents on the adsorption process. *J. Environ. Manag.* **2020**, 266. [[CrossRef](#)]
16. David, L.; Moldovan, B. Green synthesis of biogenic silver nanoparticles for efficient catalytic removal of harmful organic dyes. *Nanomaterials* **2020**, *10*, 202. [[CrossRef](#)] [[PubMed](#)]
17. Ali, E.M.; Abdallah, B.M. Effective inhibition of candidiasis using an eco-friendly leaf extract of *calotropis-gigantea*-mediated silver nanoparticles. *Nanomaterials* **2020**, *10*, 422. [[CrossRef](#)] [[PubMed](#)]
18. Sharifi-Rad, M.; Pohl, P. Synthesis of biogenic silver nanoparticles (Agcl-nps) using a *pulicaria vulgaris* gaertn. aerial part extract and their application as antibacterial, antifungal and antioxidant agents. *Nanomaterials* **2020**, *10*, 638. [[CrossRef](#)]
19. Wu, Z.; Ferreira, D.F.; Crudo, D.; Bosco, V.; Stevanato, L.; Costale, A.; Cravotto, G. Plant and biomass extraction and valorisation under hydrodynamic cavitation. *Processes* **2019**, *7*, 965. [[CrossRef](#)]
20. Ribeiro, R.P.P.L.; Barreto, J.; Xavier, M.D.G.; Martins, D.; Esteves, A.A.C.; Branco, M.; Tirolen, T.; Mota, J.P.B.; Bonfait, G. Cryogenic Neon Adsorption on Co₃(ndc)₃(dabco) Metal-Organic Framework. *Microporous Mesoporous Mater.* **2020**, *3*, 110055. [[CrossRef](#)]
21. Gene, M. Enhanced Silver Nanoparticle Synthesis by *Escherichia Coli* Transformed with *Candida Albicans*. *Materials* **2019**, *12*, 4180.
22. Catalysis, R.; Yu, C.; Tang, J.; Liu, X.; Ren, X.; Zhen, M. Green Biosynthesis of Silver Nanoparticles Using *Eriobotrya japonica* (Thunb) Leaf Extract for reductive catalysis. *Materials* **2019**, *12*, 189. [[CrossRef](#)]
23. Chemat, F.; Abert Vian, M.; Fabiano-Tixier, A.S.; Nutrizio, M.; Režek Jambrak, A.; Munekata, P.E.S.; Lorenzo, J.M.; Barba, F.J.; Binello, A.; Cravotto, G. A review of sustainable and intensified techniques for extraction of food and natural products. *Green Chem.* **2020**, *22*, 2325–2353. [[CrossRef](#)]
24. Fakhri, A.; Tahami, S.; Nejad, P.A. Preparation and characterization of Fe₃O₄-Ag₂O quantum dots decorated cellulose nanofibers as a carrier of anticancer drugs for skin cancer. *J. Photochem. Photobiol. B Biol.* **2017**, *175*, 83–88. [[CrossRef](#)] [[PubMed](#)]

25. Naeimi, H.; Nazifi, Z.S.; Amininezhad, S.M. Preparation of Fe₃O₄ encapsulated-silica sulfonic acid nanoparticles and study of their in vitro antimicrobial activity. *J. Photochem. Photobiol. B Biol.* **2015**, *149*, 180–188. [[CrossRef](#)] [[PubMed](#)]
26. Marimón-Bolívar, W.; González, E.E. Green synthesis with enhanced magnetization and life cycle assessment of Fe₃O₄ nanoparticles. *Environ. Nanotechnol. Monit. Manag.* **2018**, *9*, 58–66. [[CrossRef](#)]
27. Prasad, C.; Krishna Murthy, P.; Hari Krishna, R.H.; Sreenivasa Rao, R.; Suneetha, V.; Venkateswarlu, P. Bio-inspired green synthesis of RGO/Fe₃O₄ magnetic nanoparticles using *Murrayakoenigii* leaves extract and its application for removal of Pb(II) from aqueous solution. *J. Environ. Chem. Eng.* **2017**, *5*, 4374–4380. [[CrossRef](#)]
28. Beyene, H.D.; Werkneh, A.A.; Bezabh, H.K.; Ambaye, T.G. Synthesis paradigm and applications of silver nanoparticles (AgNPs), a review. *Sustain. Mater. Technol.* **2017**, *13*, 18–23. [[CrossRef](#)]
29. Li, W.H.; Yang, N. Green and facile synthesis of Ag-Fe₃O₄ nanocomposites using the aqueous extract of *Crataegus pinnatifida* leaves and their antibacterial performance. *Mater. Lett.* **2016**, *162*, 157–160. [[CrossRef](#)]
30. Patra, J.K.; Baek, K.H. Green biosynthesis of magnetic iron oxide (Fe₃O₄) nanoparticles using the aqueous extracts of food processing wastes under photo-catalyzed condition and investigation of their antimicrobial and antioxidant activity. *J. Photochem. Photobiol. B Biol.* **2017**, *173*, 291–300. [[CrossRef](#)]
31. Dominguez, J.R.; Gonzalez, T.; Cuerda-Correa, E.M.; Muñoz-Peña, M.J. Combating paraben pollution in surface waters with a variety of photocatalyzed systems: Looking for the most efficient technology. *Open Chem.* **2019**, *17*, 1317–1327. [[CrossRef](#)]
32. González, T.; Dominguez, J.R.; Cuerda-Correa, E.M.; Correia, S.E.; Donoso, G. Selecting and improving activated homogeneous catalytic processes for pollutant removal. Kinetics, mineralization and optimization. *J. Environ. Manag.* **2020**, *256*. [[CrossRef](#)] [[PubMed](#)]
33. Fernández-perales, M.; Rozalen, M.; Sánchez-polo, M.; Rivera-utrilla, J.; López-ramón, M.V.; Álvarez, M.A. Solar degradation of sulfamethazine using RGO/Bi composite photocatalysts. *Catalysts* **2020**, *10*, 573. [[CrossRef](#)]
34. Moreno-Castilla, C.; López-Ramón, M.V.; Fontecha-Cámara, M.Á.; Álvarez, M.A.; Mateus, L. Removal of phenolic compounds from water using copper ferrite nanosphere composites as fenton catalysts. *Nanomaterials* **2019**, *9*, 901. [[CrossRef](#)]
35. Peluso, A.; Gargiulo, N.; Aprea, P.; Pepe, F.; Peluso, A.; Gargiulo, N.; Aprea, P.; Pepe, F.; Peluso, A.; Gargiulo, N.; et al. Nanoporous Materials as H₂S Adsorbents for Biogas Purification: A Review. *Sep. Purif. Rev.* **2018**, *00*, 1–12. [[CrossRef](#)]
36. Tabatabai Yazdi, S.; Iranmanesh, P.; Saeednia, S.; Mehran, M. Structural, optical and magnetic properties of Mn_xFe_{3-x}O₄ nanoferrites synthesized by a simple capping agent-free coprecipitation route. *Mater. Sci. Eng. B Solid-State Mater. Adv. Technol.* **2019**, *245*, 55–62. [[CrossRef](#)]
37. Andrzejewski, B.; Bednarski, W.; Kaźmierczak, M.; Łapiński, A.; Pogorzelec-Glaser, K.; Hilczer, B.; Jurga, S.; Nowaczyk, G.; Załęski, K.; Matczak, M.; et al. Magnetization enhancement in magnetite nanoparticles capped with alginic acid. *Compos. Part B Eng.* **2014**, *64*, 147–154. [[CrossRef](#)]
38. Scardi, P.; Ermrich, M.; Fitch, A.; Huang, E.W.; Jardin, R.; Kuzel, R.; Leineweber, A.; Mendoza Cuevas, A.; Misture, S.T.; Rebuffi, L.; et al. Size-strain separation in diffraction line profile analysis. *J. Appl. Crystallogr.* **2018**, *51*, 831–843. [[CrossRef](#)] [[PubMed](#)]
39. Sen, R.; Das, G.C.; Mukherjee, S. X-ray diffraction line profile analysis of nano-sized cobalt in silica matrix synthesized by sol-gel method. *J. Alloys Compd.* **2010**, *490*, 515–523. [[CrossRef](#)]
40. Mittal, M.; Gupta, A.; Pandey, O.P. Role of oxygen vacancies in Ag/Au doped CeO₂ nanoparticles for fast photocatalysis. *Sol. Energy* **2018**, *165*, 206–216. [[CrossRef](#)]
41. Yadav, S.; Asthana, A.; Chakraborty, R.; Jain, B.; Singh, A.K.; Carabineiro, S.A.C.; Susan, M.A.B.H. Cationic dye removal using novel magnetic/activated charcoal/β-cyclodextrin/alginate polymer nanocomposite. *Nanomaterials* **2020**, *10*, 170. [[CrossRef](#)]
42. De Jesus Ruiz-Baltazar, Á. Green Composite Based on Silver Nanoparticles Supported on Diatomaceous Earth: Kinetic Adsorption Models and Antibacterial Effect. *J. Clust. Sci.* **2018**, *29*, 509–519. [[CrossRef](#)]
43. Shebanova, O.N.; Lazor, P. Raman spectroscopic study of magnetite (FeFe₂O₄): A new assignment for the vibrational spectrum. *J. Solid State Chem.* **2003**, *174*, 424–430. [[CrossRef](#)]
44. Jubb, A.M.; Allen, H.C. Vibrational spectroscopic characterization of hematite, maghemite, and magnetite thin films produced by vapor deposition. *ACS Appl. Mater. Interfaces* **2010**, *2*, 2804–2812. [[CrossRef](#)]

45. Vanhecke, D.; Crippa, F.; Lattuada, M.; Balog, S.; Rothen-Rutishauser, B.; Petri-Fink, A. Characterization of the shape anisotropy of superparamagnetic iron oxide nanoparticles during thermal decomposition. *Materials (Basel)*. **2020**, *13*, 2018. [[CrossRef](#)] [[PubMed](#)]
46. Huacalco, Y.; Álvarez-Torrellas, S.; Marín, M.P.; Gil, M.V.; Larriba, M.; Águeda, V.I.; Ovejero, G.; García, J. Magnetic Fe₃O₄/multi-walled carbon nanotubes materials for a highly efficient depletion of diclofenac by catalytic wet peroxideoxidation. *Environ. Sci. Pollut. Res.* **2019**, *26*, 22372–22388. [[CrossRef](#)] [[PubMed](#)]
47. Hekmatara, H.; Seifi, M.; Forooraghi, K. Microwave absorption property of aligned MWCNT/Fe₃O₄. *J. Magn. Mater.* **2013**, *346*, 186–191. [[CrossRef](#)]
48. Zhou, X.; Shi, Y.; Ren, L.; Bao, S.; Han, Y.; Wu, S.; Zhang, H.; Zhong, L.; Zhang, Q. Controllable synthesis, magnetic and biocompatible properties of Fe₃O₄ and α -Fe₂O₃ nanocrystals. *J. Solid State Chem.* **2012**, *196*, 138–144. [[CrossRef](#)]
49. Qin, Y.; Zhang, H.; Tong, Z.; Song, Z.; Chen, N. A facile synthesis of Fe₃O₄@SiO₂@ZnO with superior photocatalytic performance of 4-nitrophenol. *J. Environ. Chem. Eng.* **2017**, *5*, 2207–2213. [[CrossRef](#)]
50. Ajmal, A.; Majeed, I.; Malik, R.N.; Idriss, H.; Nadeem, M.A. Principles and mechanisms of photocatalytic dye degradation on TiO₂ based photocatalysts: A comparative overview. *RSC Adv.* **2014**, *4*, 37003–37026. [[CrossRef](#)]
51. Patel, J.; Singh, A.K.; Carabineiro, S.A.C. Assessing the photocatalytic degradation of fluoroquinolone norfloxacin by Mn:ZnS quantum dots: Kinetic study, degradation pathway and influencing factors. *Nanomaterials* **2020**, *10*, 964. [[CrossRef](#)]
52. Wang, N.; Zheng, T.; Zhang, G.; Wang, P. A review on Fenton-like processes for organic wastewater treatment. *J. Environ. Chem. Eng.* **2016**, *4*, 762–787. [[CrossRef](#)]
53. Zazouli, M.A.; Ghanbari, F.; Yousefi, M.; Madihi-Bidgoli, S. Photocatalytic degradation of food dye by Fe₃O₄-TiO₂ nanoparticles in presence of peroxymonosulfate: The effect of UV sources. *J. Environ. Chem. Eng.* **2017**, *5*, 2459–2468. [[CrossRef](#)]
54. Montañez, J.P.; Heredia, C.L.; Sham, E.L.; Farfán Torres, E.M. Photodegradation of herbicide Metsulfuron-methyl with TiO₂ supported on magnetite particles coated with SiO₂. *J. Environ. Chem. Eng.* **2018**, *6*, 7402–7410. [[CrossRef](#)]
55. Chakraborty, R.; Asthana, A.; Singh, A.K.; Yadav, S.; Susan, M.A.B.H.; Carabineiro, S.A.C. Intensified elimination of aqueous heavy metal ions using chicken feathers chemically modified by a batch method. *J. Mol. Liq.* **2020**, *312*, 113475. [[CrossRef](#)]
56. Du, T.; Zhou, L.F.; Zhang, Q.; Liu, L.Y.; Li, G.; Luo, W.B.; Liu, H.K. Mesoporous structured aluminaosilicate with excellent adsorption performances for water purification. *Sustain. Mater. Technol.* **2018**, *18*, e00080. [[CrossRef](#)]
57. Wen, T.; Wang, J.; Li, X.; Huang, S.; Chen, Z.; Wang, S.; Hayat, T.; Alsaedi, A.; Wang, X. Production of a generic magnetic Fe₃O₄ nanoparticles decorated tea waste composites for highly efficient sorption of Cu(II) and Zn(II). *J. Environ. Chem. Eng.* **2017**, *5*, 3656–3666. [[CrossRef](#)]
58. Singh, K.K.; Senapati, K.K.; Sarma, K.C. Synthesis of superparamagnetic Fe₃O₄ nanoparticles coated with green tea polyphenols and their use for removal of dye pollutant from aqueous solution. *J. Environ. Chem. Eng.* **2017**, *5*, 2214–2221. [[CrossRef](#)]
59. Ou, J.; Mei, M.; Xu, X. Magnetic adsorbent constructed from the loading of amino functionalized Fe₃O₄ on coordination complex modified polyoxometalates nanoparticle and its tetracycline adsorption removal property study. *J. Solid State Chem.* **2016**, *238*, 182–188. [[CrossRef](#)]
60. Atta, A.M. Antimicrobial Activity of Hybrids Terpolymers Based on Magnetite Hydrogel Nanocomposites. *Materials* **2019**, *12*, 3604.
61. Xia, Q.H.; Ma, Y.J.; Wang, J.W. Biosynthesis of silver nanoparticles using *Taxus yunnanensis* callus and their antibacterial activity and cytotoxicity in human cancer cells. *Nanomaterials* **2016**, *6*, 160. [[CrossRef](#)] [[PubMed](#)]
62. Vázquez Olmos, A.R.; Vega Jiménez, A.L.; Paz Díaz, B. Mecanó-síntesis y efecto antimicrobiano de óxidos metálicos nanoestructurados. *Mundo Nano Rev. Interdiscip. Nanocienc. Nanotecnol.* **2018**, *11*, 29. [[CrossRef](#)]

